

A novel method for testing isotropy with Shannon entropy

Biswajit Pandey[★]

Department of Physics, Visva-Bharati University, Santiniketan, Birbhum, 731235, India

22 November 2018

ABSTRACT

We propose a novel method for testing isotropy of a three-dimensional distribution using Shannon entropy. We test the method on some Monte Carlo simulations of isotropic and anisotropic distributions and find that the method can effectively identify and characterize different types of hemispherical asymmetry inputted in a distribution. We generate anisotropic distributions by introducing pockets of different densities inside homogeneous and isotropic distributions and find that the proposed method can effectively quantify the degree of anisotropy and determine the geometry of the pockets introduced. We also considered spherically symmetric radially inhomogeneous distributions which are anisotropic at all points other than the centre and find that such anisotropy can be easily characterized by our method. We use a semi analytic galaxy catalogue from the Millennium simulation to study the anisotropies induced by the redshift space distortions and find that the method can separate such anisotropies from a general one. The method may be also suitably adapted for any two dimensional maps on the celestial sphere to study the hemispherical asymmetry in other cosmological observations.

Key words: methods: numerical - galaxies: statistics - cosmology: theory - large scale structure of the Universe.

1 INTRODUCTION

The Cosmological principle which assumes that the Universe is statistically homogeneous and isotropic on large scales is the foundation of modern cosmology. This assumption which was originally introduced by Albert Einstein considerably simplifies the study of the large scale structure of the Universe. The assumption can not be proved in a rigorously mathematical sense but can be verified from various cosmological observations. Homogeneity and isotropy are two different but related aspects of a system which may or may not coexist. For instance the Universe can be homogeneous without being isotropic or can be isotropic around a point without being homogeneous. But isotropy around each and every point guarantees homogeneity.

Observationally the most powerful evidence for isotropy is provided by the near uniform temperature of the Cosmic Microwave Background Radiation (CMBR) across the whole sky (Penzias & Wilson 1965; Smoot et al. 1992; Fixsen et al. 1996). However the CMBR is not completely isotropic. Over the years many studies have reported power asymmetries and unlikely alignments of low multipoles (Schwarz et al. 2004; Land & Magueijo 2005;

Hanson & Lewis 2009; Moss et al. 2011; Gruppuso et al. 2013; Dai et al. 2013). The asymmetries found in WMAP were largely attributed to deficiencies in the foreground subtraction (Bennett et al. 2011) and non circularity of beams (Das et al. 2014). However recent analysis of PLANCK data by Planck Collaboration et al. (2014) reported that the power asymmetry persist on scales corresponding to $l \sim 600$ and the deviations from isotropy are at high statistical significance ($3 - \sigma$). A further analysis using multi frequency PLANCK data by Planck Collaboration et al. (2015) confirmed the power asymmetry and show that the foreground residuals are unlikely to affect these results.

The Hubble's law which describes the observed expansion of the Universe represents the only form of expansion compatible with homogeneity and isotropy of the Universe. However the distribution of galaxies in the nearby Universe as revealed by different galaxy redshift surveys indicates that the local Universe is neither homogeneous nor isotropic and therefor deviations from Hubble flow are expected. The observed deviations from homogeneity and isotropy arise from peculiar velocities resulting from structure formation. Redshift space distortions resulting from peculiar flows introduce anisotropy in the observed clustering of galaxies which can be theoretically modelled on large scales using linear perturbation theory (Kaiser 1987; Hamilton 1992).

[★] E-mail: biswap@visva-bharati.ac.in

The bulk flows are expected to disappear on sufficiently large scales where the density fluctuations are very small. [Watkins et al. \(2009\)](#) analyzed data from a large number of peculiar velocity surveys and detect statistically significant large cosmic flows on scales of $100h^{-1}\text{Mpc}$. A combined study with the WMAP data and x-ray cluster catalog indicates strong and coherent bulk flow out to at least $\gtrsim 300h^{-1}\text{Mpc}$ ([Kashlinsky et al. 2008, 2010](#)). Such large scale bulk motion indicates that there are significant density fluctuations on very large scales. Contrary to these findings recent study of low-redshift Type-Ia Supernovae suggest no excess bulk flow on top of what is expected in ΛCDM model ([Huterer et al. 2015](#)). There would be a major paradigm shift in modern cosmology if the assumption of cosmic isotropy is ruled out with high statistical significance by multiple data sets. A large number of theoretical studies have been carried out on the possible origins of such anisotropy and their consequences. Inflation pushes any pre-inflationary anisotropies and inhomogeneities far beyond the horizon given the number of e-foldings is large. [Shtanov \(2010\)](#) calculated the theoretical expectation of statistical anisotropy from inflation. [Barrow & Hervik \(2010\)](#) calculated the level of statistical anisotropy expected from anisotropic inflation and predicted the corresponding observable anisotropy in the CMB pointing out that the resulting anisotropy will not be scale invariant and grow with scale. [Soda \(2012\)](#) formulate cosmological perturbation theory in anisotropic inflation and propose a method to test anisotropic inflation using CMB. [Pitrou et al. \(2008\)](#) predicted the primordial anisotropy in the power spectra of gravity waves and curvature perturbations from an inflationary phase starting from a homogeneous and anisotropic Universe. [Chan et al. \(2009\)](#) investigate cosmologies where the accelerated expansion of the Universe is driven by an anisotropic equation of state for dark energy. Large scale inhomogeneities through the backreaction mechanism can provide an alternate explanation of a global cosmic acceleration without requiring any additional dark energy component ([Buchert & Ehlers 1997; Buchert 2001; Kolb et al. 2006](#)). [Marozzi & Uzan \(2012\)](#) quantified the expected deviation from isotropy arising from backreaction of large scale structure and explored the possibility of constraining backreaction using late time anisotropy of the Hubble flow. [Fang & Linden \(2015\)](#) calculate the synchrotron anisotropy from dark matter annihilation which is very small even for large substructure abundance and strong magnetic fields. [Pitrou et al. \(2008\)](#) show that the origin of weak lensing B-modes on large angular scales is related to deviations from isotropy. Recently [Mukherjee et al. \(2015\)](#) investigated direction dependence of cosmological parameters due to hemispherical asymmetry using non-isotropic Gaussian random simulations and find that n_s and A_s are the most susceptible parameters to such variations in the sky.

Recently there has been a growing interest in testing the assumption of statistical isotropy precisely in the present Universe using various data sets. [Jackson \(2012\)](#) analyze a sample of ultra-compact radio sources from a 2.29 GHz VLBI all sky survey to test the isotropy of the Universe in which they determined Ω_m in different hemispherical subsamples and find significant anisotropy. [Marinoni et al. \(2012\)](#) developed a formalism to determine the scale of cosmic isotropy and applied their method to SDSS DR7 to find that the

galaxy distribution becomes statistically isotropic on a scale of $\sim 150h^{-1}\text{Mpc}$. [Hazra & Shafieloo \(2015\)](#) use the statistical moments of the probability distribution function of the Lyman-alpha forest transmitted flux from the high redshift quasars from SDSS-III BOSS-DR9 to test the isotropy and find their results consistent with isotropic distribution. [Appleby & Shafieloo \(2014\)](#) used the shape of the luminosity function to test the isotropy of the galaxy distribution in 2MASS extended source catalogue and find a dipole in the shape of the luminosity function. [Alonso et al. \(2015\)](#) studied the hemispherical asymmetries in the 2MASS photometric redshift catalogue to find no significant deviation beyond those allowed by the ΛCDM model.

Type-Ia Supernovae (SNe Ia) are regarded as the ideal distance indicator for measuring the accelerated expansion of the Universe and they have been widely used to test any anisotropy in the accelerated expansion of the Universe. [Schwarz & Weinhorst \(2007\)](#) test the isotropy of the Hubble diagram using SNe Ia data and find a statistically significant anisotropy towards the equatorial poles which they ascribe to systematics in the supernovae data. [Gupta & Saini \(2010\)](#) test the directional dependence in the supernovae data from the gold data sets and find the data consistent with isotropy. [Campanelli et al. \(2011\)](#) analyze the magnitude-redshift data of Type Ia Supernovae in the Union and Union2 in the framework of anisotropic cosmological models and find that a large level of anisotropy is allowed both in the geometry of the Universe and in the equation of state of dark energy. [Colin et al. \(2011\)](#) studied the anisotropy of the local Universe using the Union2 catalogue of Type Ia supernovae (SNe Ia) data and find that at low redshift bulk flow due to local inhomogeneities systematically bias the reconstruction history of the Universe. [Kalus et al. \(2013\)](#) test the isotropy of the expansion of the Universe by estimating the hemispherical asymmetry of Supernovae (SNe Ia) Hubble diagram at low redshifts and find hemispherical asymmetry of the Hubble expansion at 95% confidence level. [Javanmardi et al. \(2015\)](#) test the isotropy of the redshift-magnitude relation of Type Ia Supernovae (SNe Ia) in Union2.1 compilation and pointed out some discrepant directions which they ascribe to either systematics in SNe data or a failure of the assumption of isotropy. [Bengaly et al. \(2015\)](#) investigate the directional dependence of the cosmological parameters H_0 and q_0 across the celestial sphere using Union2.1 and JLA compilation of Type Ia Supernovae (SNe Ia) and conclude that the directional asymmetry are either of local origin or due to incompleteness of SNe Ia samples. [Lin et al. \(2015\)](#) test the possible anisotropy in the accelerated expansion of the Universe using JLA (Joint light-curve analysis) compilation of Type Ia Supernovae and find no significant evidence for the anisotropic expansion of the Universe.

So far many studies have been carried out on the issue of cosmic isotropy using different statistics and cosmological data sets. Different statistics has been proposed for different types of datasets. Bipolar spherical harmonics spectra of CMBR ([Hajian & Souradeep 2003](#)), Spherical harmonic decomposition of gravitational wave signals ([Taylor & Gair 2013](#)) and multipole vector decomposition for galaxy density field ([Zunckel et al. 2011](#)) are to name a few. Although large number of studies points to statistical isotropy of the Universe on large scales there is no clear consensus on this issue

yet. Different datasets are contaminated by different types of systematics and the scope of application of the same statistics on different datasets are also limited. So it is difficult to make a fair comparison between different studies.

Pandey (2013) introduce a method based on the Shannon entropy (Shannon 1948) for characterizing inhomogeneities in a 3D distribution of points and applied the method on some Monte Carlo simulations of inhomogeneous distributions and N-body simulations which show that the proposed method has great potential for testing the large scale homogeneity in galaxy redshift surveys. Recently Pandey & Sarkar (2015) applied this method to galaxy distributions from SDSS DR12 (Ahn et al. 2014) and find that the inhomogeneities in the galaxy distributions persist at least upto a length scale of $120h^{-1}$ Mpc. In the present work we propose a method for testing isotropy based on the Shannon entropy or information entropy. The proposed method can be directly applied to any 3D distributions of galaxies or the corresponding density fields derived from them. The method can be easily extended to 2D maps such as CMB and may be also suitably adapted for testing isotropy of gravitational waves, cosmic rays, X-ray or Radio Sky.

A brief outline of the paper follows. We describe our method in Section 2, describe the data and the tests in Section 3 and presents the results and conclusions in Section 4.

We have used a Λ CDM cosmological model with $\Omega_{m0} = 0.3$, $\Omega_{\Lambda 0} = 0.7$ and $h = 1$ throughout.

2 METHOD OF ANALYSIS

Pandey (2013) propose a method based on the Shannon entropy or information entropy to study inhomogeneities in a 3D distribution of points. Shannon entropy (Shannon 1948) is originally proposed by Claude Shannon to quantify the information loss while transmitting a message in a communication channel. It gives a measure of the amount of information required to describe a random variable. The Shannon entropy for a discrete random variable x with n outcomes $\{x_i : i = 1, \dots, n\}$ is a measure of uncertainty denoted by $H(X)$ defined as,

$$H(X) = - \sum_{i=1}^n p(x_i) \log p(x_i) \quad (1)$$

where $p(x)$ is the probability distribution of the random variable x .

In the present work we propose information entropy as a measure of isotropy. We assume a set of points distributed in 3D and wish to test the assumption of statistical isotropy around any point. In order to test the isotropy around a point we first uniformly bin $\cos\theta$ and ϕ where θ and ϕ are the polar angle and azimuthal angle in spherical polar coordinates respectively. Uniform binning of $\cos\theta$ and ϕ ensure equal size for each solid angle bin since $d\Omega = \sin\theta d\theta d\phi$. The number of bins m_θ and m_ϕ for binning $\cos\theta$ and ϕ are to be decided conveniently. A given choice of m_θ and m_ϕ results in a total $m_{total} = m_\theta m_\phi$ solid angle bins. We impose an upper limit to the radius r upto which the isotropy is to be tested. There is a natural limit to r from the fact that the data points are available only upto a certain radius r_{max} .

We pick up a point about which isotropy has to be tested and treating that point as origin define the coordinates of all the other points in the distribution. We bin the co-ordinates for a given choice of m_θ , m_ϕ and r . This results in $m_{total} = m_\theta m_\phi$ volume elements each covering the same solid angle. For any given value of r each of the volume elements has the same radial extension ensuring same volume $dv = \frac{r^3}{3} d\Omega$ for each of them. We count the number of points n_i inside each of the m_{total} volume elements where i is the index of the volume element. In general each galaxy within radius r from the centre can reside in only one of the m_{total} volume elements. But which volume element a particular galaxy belongs to? The answer to this question has m_{total} likely outcomes. We define a random variable $X_{\theta\phi}$ which has m_{total} possible outcomes each given by, $f_i = \frac{n_i}{\sum_{i=1}^{m_{total}} n_i}$ with the constraint $\sum_{i=1}^{m_{total}} f_i = 1$. The Shannon entropy associated with the random variable $X_{\theta\phi}$ can be written as,

$$\begin{aligned} H_{\theta\phi} &= - \sum_{i=1}^{m_{total}} f_i \log f_i \\ &= \log N - \frac{\sum_{i=1}^{m_{total}} n_i \log n_i}{N} \end{aligned} \quad (2)$$

Where N is the total number of points within radius r . The base of the logarithm is arbitrary and we choose it to be 10. f_i will have the same value $\frac{1}{m_{total}}$ for all the volume elements when n_i is same for all of them. This maximizes the Shannon entropy to $(H_{\theta\phi})_{max} = \log m_{total}$ for a given choice of m_θ, m_ϕ and any r . We define the relative Shannon entropy as the ratio of the entropy of a random variable $X_{\theta\phi}$ to the maximum possible entropy $(H_{\theta\phi})_{max}$ associated with it. The relative Shannon entropy $\frac{H_{\theta\phi}}{(H_{\theta\phi})_{max}}$ then quantifies the degree of uncertainty in the knowledge of the random variable $X_{\theta\phi}$. Equivalently $1 - \frac{H_{\theta\phi}}{(H_{\theta\phi})_{max}}$ quantify the residual information and can be treated as a measure of anisotropy. The fact that galaxies are not residing in any particular volume element and rather are spread across all of them with different probabilities acts as a source of information. If all of them would have been residing in a particular volume element then there would be no uncertainty and no information at all making $H_{\theta\phi} = 0$ or $1 - \frac{H_{\theta\phi}}{(H_{\theta\phi})_{max}} = 1$. This fully determined situation corresponds to maximum anisotropy. On the other hand when all the m_{total} volume elements are populated with equal probabilities it would be most uncertain to decide which particular volume element a galaxy belongs to. This maximizes the information entropy to $H_{\theta\phi} = \log m_{total}$ turning $1 - \frac{H_{\theta\phi}}{(H_{\theta\phi})_{max}} = 0$. This corresponds to a situation when the distribution is completely isotropic. The galaxy distribution is expected to be anisotropic on small scales but with increasing solid angle $d\Omega$ and radius r one would expect it to be isotropic on some scale provided the Cosmological principle holds on large scales. We change the value of r starting from a small radius r and gradually increase it in steps upto the maximum radius r_{max} to study how $1 - \frac{H_{\theta\phi}}{(H_{\theta\phi})_{max}}$ varies with r for a given choice of m_θ and m_ϕ . It may be noted here that the analysis can be also done for data covering parts of the sky.

Besides the radial anisotropy one can also measure the degree of polar anisotropy $1 - \frac{H_\theta}{(H_\theta)_{max}}$ and the azimuthal anisotropy $1 - \frac{H_\phi}{(H_\phi)_{max}}$ as function of θ and ϕ by carrying out the sum respectively over m_ϕ or m_θ instead of m_{total} in

Equation 2. Note that in this case N would be the total number of points inside all the m_ϕ or m_θ volume elements at different θ or ϕ respectively. The anisotropies can be also easily calculated for any given theoretical distribution $\rho(r, \theta, \phi)$. One can determine n_i and N by carrying out the integral $\int \int \int \rho(r, \theta, \phi) r^2 \sin \theta d\theta d\phi$ over appropriate r, θ and ϕ range and use them in **Equation 2** to calculate the anisotropies.

The method presented here can be directly applied to different galaxy redshift surveys to test the isotropy of the galaxy distributions in the present Universe. The redshift surveys map the mass distribution on a light cone time slice where the distribution does not evolve much over the light crossing time of the survey. But for very large galaxy surveys possible evolutionary effects can introduce signatures of anisotropy in the data. Redshift dependent selection effects can also introduce artificial anisotropy in the data. Besides these the redshift space distortions is one of the most important source of anisotropy in galaxy surveys. On large scales structures are compressed along the line of sight due to coherent flows into overdense regions and out of underdense regions whereas on small scales structures are elongated along the line of sight by random motions in virialized clusters. The volume elements used for measurement of n_i in our method radially extends along the line of sight where the radial extension is much larger compared to their angular width. When measurements are done from the point from which observations are carried out one would expect uniformity in the measurement of n_i across all directions for large r provided the Universe is isotropic. But this would appear anisotropic if one shifts the origin from the point of observation given such sources of anisotropies are present. It is important to distinguish the presence of genuine anisotropies from the artificial ones such as introduced by radial inhomogeneities (due to selection effects, evolutionary effects) and redshift space distortions. We will show that our method can distinguish the signatures of different kind of anisotropies present in the distribution.

The method presented here has a significant advantage compared to the method proposed by [Pandey \(2013\)](#) for testing homogeneity using Shannon entropy. The volume elements used for measuring the number count n_i in this method do not overlap. Consequently all the complexities due to overlap can be bypassed allowing one to have a more direct and clear interpretation.

3 TESTING THE METHOD

In order to study the prospects and limitations of the proposed method we carry out some preliminary tests by applying it to some simple distributions. We consider the following distributions: (1) homogeneous and isotropic Poisson distributions, (2) anisotropic distributions generated by inserting pockets of different densities at different locations in homogeneous and isotropic Poisson distributions, (3) radially inhomogeneous Poisson distributions which are isotropic only about one point i.e. the centre and (4) simulated galaxy distributions from N-body simulations in real space and redshift space.

For the first three types we generate a set of Monte Carlo realizations. The distributions of type (1) are isotropic and type (2) are anisotropic by construction. The distribu-

tions of type (3) are radially inhomogeneous and the radial variations are identical in all directions making them isotropic about the centre of the sphere. But if we shift the origin from the centre of the sphere the distribution would appear anisotropic and the degree of anisotropy would depend on the magnitude and direction of the shift in a predictable manner. For the distributions of type (4) we use the data from a semi analytic galaxy catalogue from the Millennium simulation. An isotropic distribution in real space would appear anisotropic in redshift space due to redshift space distortions induced by the peculiar velocities. We map the particles in N-body simulations from real space to redshift space using their peculiar velocities and measure the resulting anisotropies induced by redshift space distortions. In all cases we have considered a spherical region of radius $200h^{-1}$ Mpc.

We analyze the datasets separately using the method described in section 2. We divide the $\theta - \phi$ space into $m_\theta m_\phi$ solid angle bins where m_θ and m_ϕ are variables and chosen conveniently. The following calculations are carried out for each of the datasets described in the subsections below.

(i) We choose the minimum and maximum values of radius r to be $r_{min} = 5h^{-1}$ Mpc and $r_{max} = 200h^{-1}$ Mpc. We gradually increase the radius r in steps of $5h^{-1}$ Mpc from r_{min} to r_{max} and compute the Shannon entropy $\frac{H_{\theta\phi}}{(H_{\theta\phi})_{max}}$ for each radius using all the available $m_\theta m_\phi$ bins.

(ii) We fix the radius at $r_{max} = 200h^{-1}$ Mpc and compute $\frac{H_\theta}{(H_\theta)_{max}}$ for each θ using all the m_ϕ azimuthal bins available.

(iii) We fix the radius at $200h^{-1}$ Mpc and compute $\frac{H_\phi}{(H_\phi)_{max}}$ for each ϕ using all the m_θ polar bins available.

(iv) We shift the origin by $100h^{-1}$ Mpc along the x-axes without any rotation and repeat (i),(ii) and (iii) using $r_{max} = 100h^{-1}$ Mpc.

(v) We shift the origin by $100h^{-1}$ Mpc along the y-axes without any rotation and repeat (i),(ii) and (iii) using $r_{max} = 100h^{-1}$ Mpc.

(vi) We shift the origin by $100h^{-1}$ Mpc along the z-axes without any rotation and repeat (i),(ii) and (iii) using $r_{max} = 100h^{-1}$ Mpc.

In general one can apply the shift along any arbitrary directions and it would not make any difference given the distribution is isotropic. Further if one can verify the isotropy around other points it would also help us in testing homogeneity of the distribution.

3.1 MONTE CARLO SIMULATIONS

The Monte Carlo simulations for the data sets of type (1) and (3) are generated by considering two simple radial density distributions $\rho(r, \theta, \phi) = K \lambda(r)$ where $\lambda(r) = 1$ for type (1) and $\lambda(r) = \frac{1}{r^2}$ for type (3) distributions. Here K is a normalization constant. The type (1) distributions are homogeneous and isotropic Poisson point process which has a constant density everywhere. The type (3) distributions are radially inhomogeneous Poisson distributions which are isotropic only about the centre.

Enforcing the desired number of particles N within radius R one can turn the radial density function into a probability function within $r = 0$ to $r = R$ which is normalized to one when integrated over that interval. So the probability of

finding a particle at a given radius r is $P(r) = \frac{r^2 \lambda(r)}{\int_0^R r^2 \lambda(r) dr}$ which is proportional to the density at that radius implying more particles in high density regions.

We generate the Monte Carlo realizations of these distributions using a Monte Carlo dartboard technique. The maxima of the function $r^2 \lambda(r)$ in $P(r)$ is at $r = R$ for type (1) distribution whereas in type (3) distribution it is same and constant everywhere. We label the maximum value of $P(r)$ as P_{max} . We randomly choose a radius r in the range $0 \leq r \leq R$ and a probability value is randomly chosen in the range $0 \leq P(x) \leq P_{max}$. The actual probability of finding a particle at the selected radius is then calculated using expression for $P(r)$ and compared to the randomly selected probability value. If the random probability is less than the calculated value, the radius is accepted and assigned isotropically selected angular co-ordinates θ and ϕ , otherwise the radius is discarded. In this way, radii at which particle is more likely to be found will be selected more often because the random probability will be more frequently less than the calculated actual probability. We choose $R = 200h^{-1}$ Mpc and $N = 10^5$.

To generate the distributions of type (2) we first generate a homogeneous and isotropic Poisson distribution within a spherical region of radius $200h^{-1}$ Mpc with $N = 10^5$. We randomly identify a region in (r, θ, ϕ) space assuming the centre of the sphere as origin. We discard all the data points from the selected region and subsequently populate it with a homogeneous and isotropic Poisson distribution having a different intensity parameter than the original one. As a result this region will have a different mean density which introduces a preferred direction and hence anisotropy in the distribution.

We generate 10 realizations for each of the above density distributions and analyze them separately using the method described earlier.

3.2 MILLENNIUM SIMULATION

Semi analytic models (White & Frenk 1991; Kauffmann, White & Guiderdoni 1993; Kauffmann & White 1993; Kauffmann 1996; Cole et al. 1994, 2000; Somerville & Primack 1999; Baugh et al. 1998; Benson et al. 2002; Springel et al. 2005; Guo et al. 2011) provide a very powerful tool to study galaxy formation and evolution. Galaxy formation and evolution involve many physical processes such as gas cooling, star formation, supernovae feedback, metal enrichment, merging and morphological evolution. The semi analytic models parametrise the physics involved in terms of simple models following the dark matter merger trees over time. The models provide the statistical predictions of galaxy properties at some epoch and the precision of these predictions are directly related to the accuracy of the input physics. In the present work we use a semi-analytic galaxy catalogue generated by Guo et al. (2011) from the Millennium Run simulation (Springel et al. 2005) who updated the previously available galaxy formation models (Springel et al. 2005; Croton et al. 2006; De Lucia & Blaizot 2007) with improved versions. The spectra and magnitude of the model galaxies were computed using population synthesis models of Bruzual & Charlot (2003). We place the origin at the centre of the simulation box which has a length of

$500h^{-1}$ Mpc on each side and then identify all the galaxies within a radius of $200h^{-1}$ Mpc having r-band Petrosian absolute magnitude in the range $-22 \leq M_r \leq -20$. We randomly select 10^5 galaxies from them to construct the simulated galaxy sample in real space for our analysis. We then map these galaxies to redshift space using their peculiar velocities to obtain their distribution in redshift space.

4 RESULTS AND CONCLUSIONS

We show the results for the homogeneous and isotropic Poisson distributions in Figure 1. In top left, middle left and bottom left panels we show the degree of anisotropies as a function of r , θ and ϕ respectively. The top left panel shows the variations of $1 - \frac{H_{\theta\phi}}{(H_{\theta\phi})_{max}}$ (hereafter radial anisotropy) as a function of r for different choices of m_θ and m_ϕ . At the smallest radius one finds a large anisotropy arising purely from Poisson noise which gradually diminishes with increasing radii. This result holds for all choices of m_θ and m_ϕ but for larger values of m_θ and m_ϕ the anisotropies resulting from Poisson noise are larger and persist upto larger length scales. This arises simply because with increasing m_θ and m_ϕ the solid angle bins cover smaller volumes and hence contain fewer points within for any given r . The middle left panel shows the variations of $1 - \frac{H_\theta}{(H_\theta)_{max}}$ (hereafter polar anisotropy) as a function of θ for different choices of m_θ and m_ϕ labeled in the panel. We note that for $m_\theta = 10$ and $m_\phi = 20$ we uniformly get $1 - \frac{H_\theta}{(H_\theta)_{max}} = 0$ for all values of θ indicating isotropy of the distribution. But as we increase the total number of bins by 10^2 times ($m_\theta = 100, m_\phi = 200$) and 10^4 times ($m_\theta = 1000, m_\phi = 2000$) the anisotropies resulting from the Poisson noise become evident. The degree of anisotropy increases with increasing number of bins for all θ but does not change with θ indicating a systematic behaviour as expected from Poisson noise. We notice exactly same behaviour for $1 - \frac{H_\phi}{(H_\phi)_{max}}$ (hereafter azimuthal anisotropy) as a function of ϕ in the bottom left panel confirming isotropy of the distribution. The Poisson character of the anisotropy can be also clearly seen here when the number of bins are increased by 2 and 4 orders of magnitude.

In the top right, middle right and bottom right panels we show how the anisotropies vary with r , θ and ϕ respectively for different choices of m_θ and m_ϕ when the origin is shifted by $100h^{-1}$ Mpc along the x or y or z axes without any rotation. It may be noted here that we can only probe upto a length scale of $100h^{-1}$ Mpc under these circumstances. We set $r_{max} = 100h^{-1}$ Mpc in each of these cases. In the top right panel we see that the $1 - \frac{H_{\theta\phi}}{(H_{\theta\phi})_{max}}$ remain unaltered when the origin is shifted by $100h^{-1}$ Mpc along the x, y and z axes or not shifted at all indicating the isotropy of the distribution. This result holds for each set of m_θ and m_ϕ . In the right middle panel we show $1 - \frac{H_\theta}{(H_\theta)_{max}}$ as a function of θ when the origin is not shifted and when the origin is shifted along three different directions. Interestingly the results overlap with each other again pointing towards isotropy of the distribution. One may note here that the degree of anisotropy and the size of the errorbars increase at a fixed choice of m_θ and m_ϕ due to the decrease in r_{max} resulting in a smaller

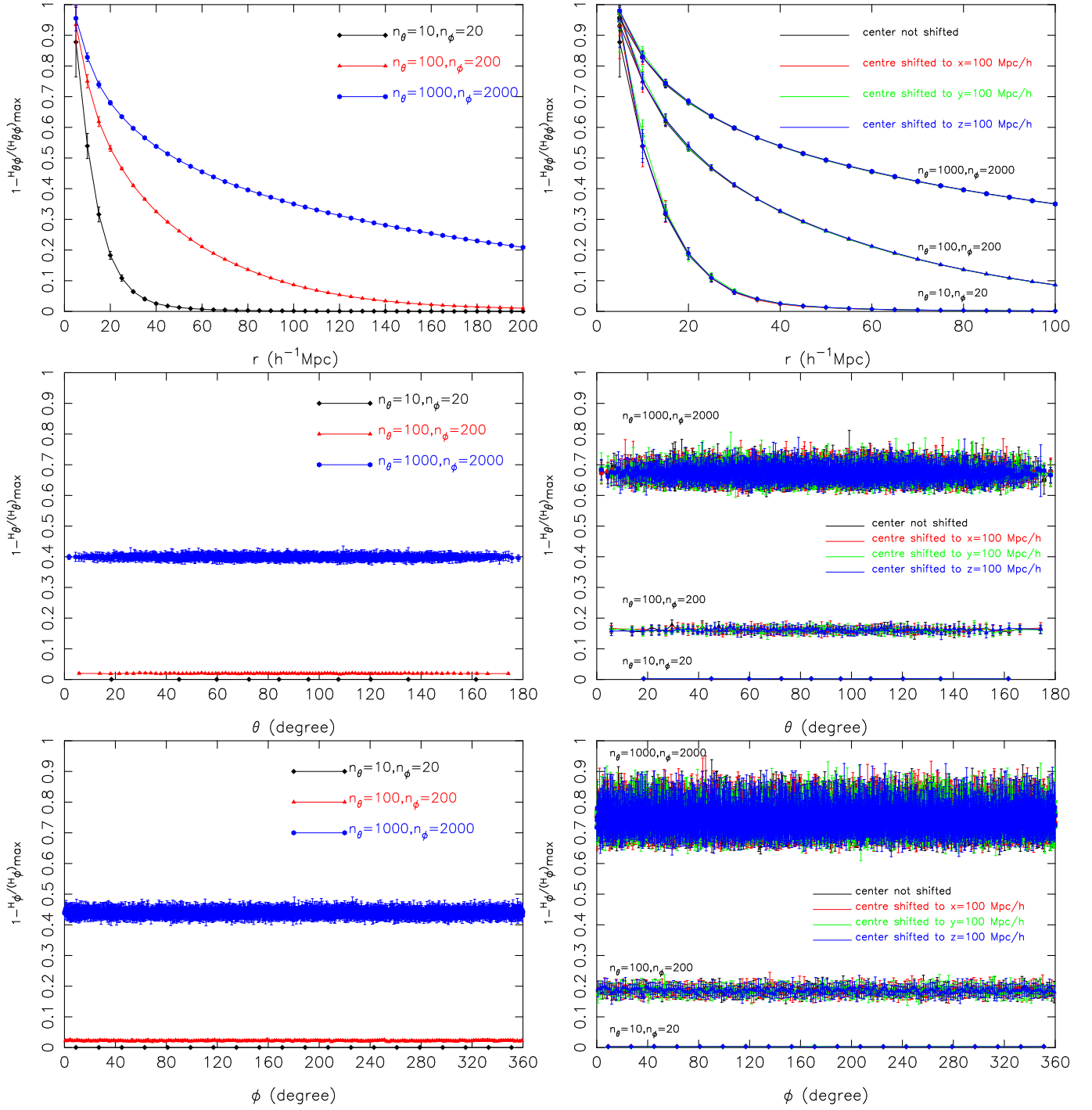


Figure 1. The top left, middle left and bottom left panels show the measured anisotropies in a homogeneous and isotropic Poisson distribution as functions of r , θ and ϕ respectively for different choices of m_θ and m_ϕ as labeled in each panel. The top right, middle right and bottom right panels show the same quantities when the origin is shifted along x or y or z directions from the centre by $100h^{-1}$ Mpc. We use $r_{max} = 200h^{-1}$ Mpc and $r_{max} = 100h^{-1}$ Mpc for all the panels on left and right respectively. The error-bars shown here in all the panels are the $1-\sigma$ variations from the 10 Monte Carlo realizations used in each case.

number of points within the volumes analyzed. In the bottom right panel $1 - \frac{H_\phi}{(H_\phi)_{max}}$ as a function of ϕ shows identical behaviour showing isotropy of the distribution in ϕ and rise in anisotropy with increase in the number of bins. Here the error bars are derived from 10 different Monte Carlo realizations in each case. We are interested in finding out the genuine signals of anisotropy. So keeping in mind the role

of Poisson noise in increasing the anisotropy and the size of error-bars we decide to use $m_\theta = 10$ and $m_\phi = 20$ for the rest of our analysis. One can of course safely increase m_θ and m_ϕ by increasing the density of the distribution at the same time.

We introduce an empty pocket in the homogeneous and isotropic Poisson distribution by removing all the points

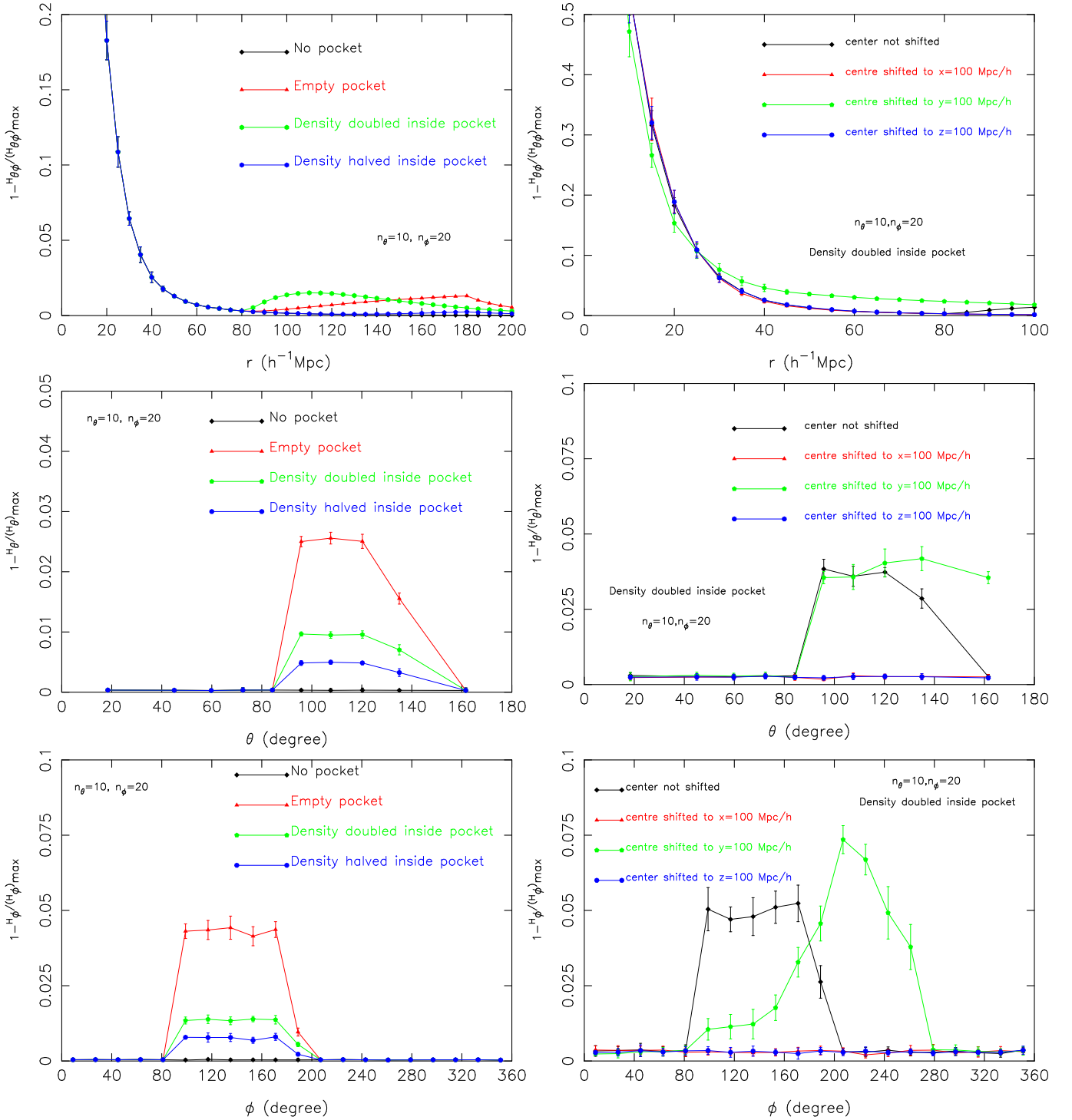


Figure 2. Same as Figure 1. but for anisotropic Poisson distribution obtained by introducing pocket of different density in a homogeneous and isotropic Poisson distribution. Only the results for $m_{\theta} = 10$ and $m_{\phi} = 20$ are shown in each panel.

from the region $80h^{-1}\text{Mpc} \leq r \leq 180h^{-1}\text{Mpc}$, $90^{\circ} \leq \theta \leq 140^{\circ}$ and $90^{\circ} \leq \phi \leq 190^{\circ}$. This introduces a directional asymmetry in the resulting distribution. Subsequently we fill up the empty pocket by generating another homogeneous and isotropic Poisson distribution within it which has a different density than the original one. We considered two distinct case, one in which we doubled the density and another in which we halved the density with respect to the original dis-

tribution. We analyze 10 such Monte Carlo realizations in each case. The results are shown in Figure 2. We show the radial anisotropy as a function of r for $m_{\theta} = 10$ and $m_{\phi} = 20$ in the top left panel of Figure 2. As seen earlier in Figure 1 once again we see a higher degree of anisotropy on small scales due to the Poisson noise. The anisotropy decreases with increasing length scales when there is no pocket in the distribution. But in the presence of the pocket described

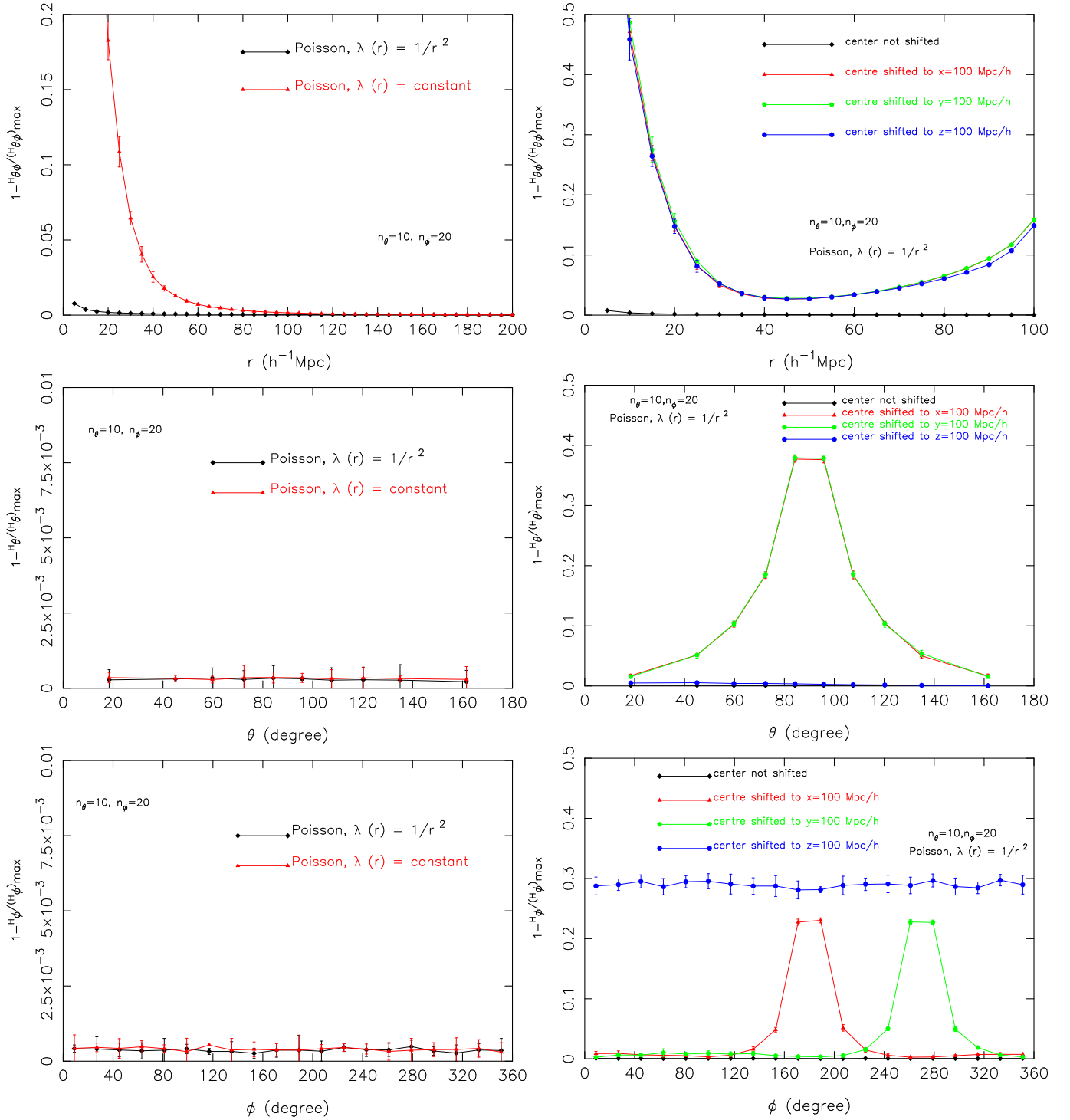


Figure 3. Same as Figure 1. but for radially inhomogeneous Poisson distribution where density varies as $\frac{1}{r^2}$ from the centre. Only the results for $m_\theta = 10$ and $m_\phi = 20$ are shown in each panel.

above the anisotropies reappear again at $80h^{-1}$ Mpc and persists thereafter. It may be noted here that the pocket introduced radially extends from $80h^{-1}$ Mpc to $180h^{-1}$ Mpc from the centre. We note that the signals of anisotropy in this range of radii are less pronounced when the density of points are halved than when doubled or when the pocket is left empty. The left middle and left bottom panel show the polar anisotropy as a function of θ and azimuthal anisotropy

as a function of ϕ respectively. In the left middle panel we see a clear and distinct bump in the polar anisotropy in the θ range 90° to 160° when the pocket is introduced in the distribution. Noticeably the bump is absent when no such pockets are introduced. For all other θ values we uniformly get $1 - \frac{H_\theta}{(H_\theta)_{\max}} = 0$. The height of the bump quantifies the degree of anisotropy and depends on the number density inside the pocket. The bump clearly indicates violation of isotropy

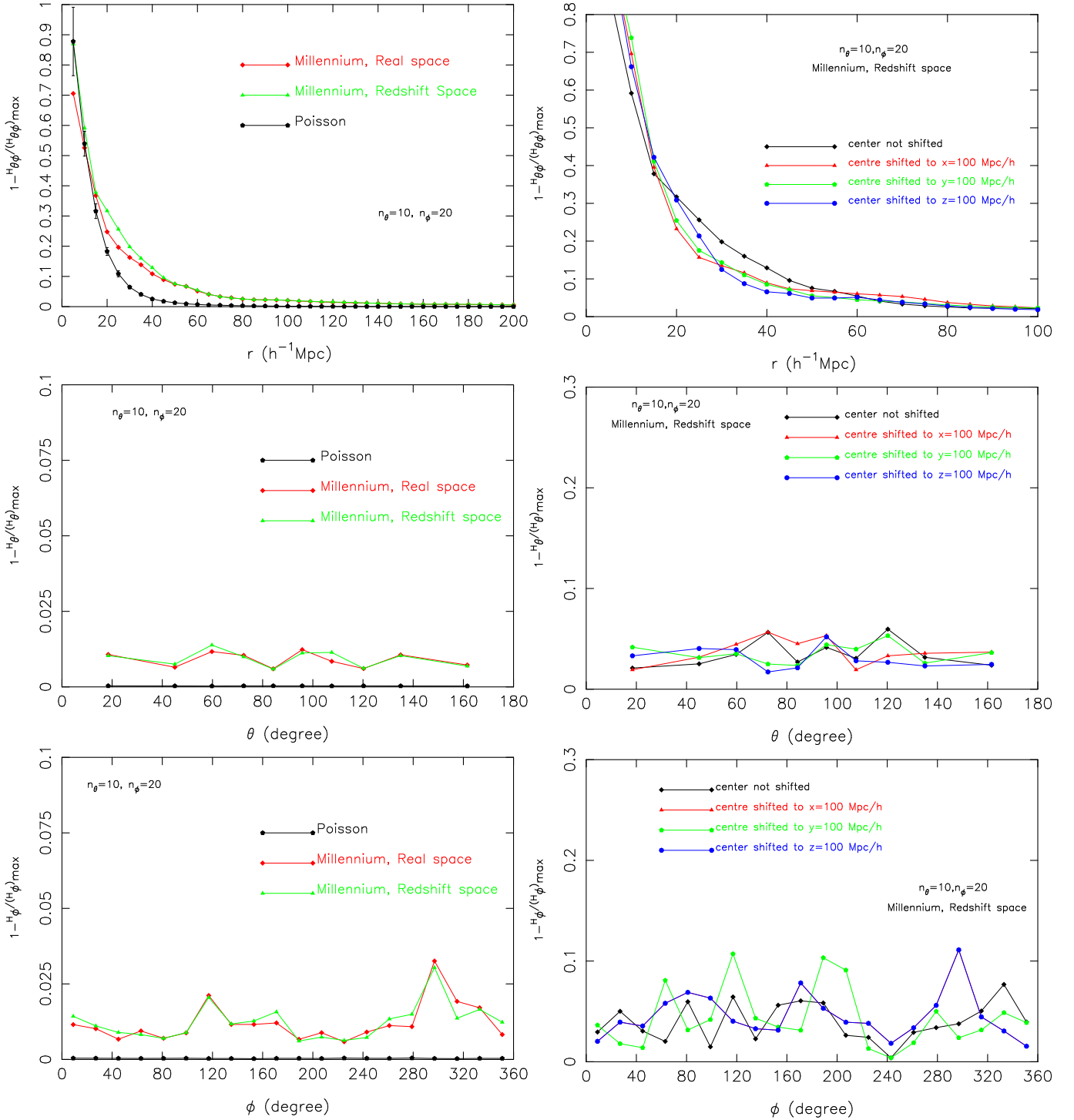


Figure 4. Same as Figure 1. but for simulated galaxy distributions from a semi analytic galaxy catalogue from the Millennium Run simulation. The panels on left side compares the results for the real space and redshift space whereas the panels on right only show the results for the redshift space. Only the results for $m_\theta = 10$ and $m_\phi = 20$ are shown in each panel.

in the range of θ values over which it appears. Interestingly the pocket generated spans exactly the same range of θ over which the bump appears. Consequently one can infer the size of the pocket from the features of the bump. The fact that the bumps extend upto $160h^{-1}$ Mpc rather $140h^{-1}$ Mpc is due to the fact the next θ bin after 135° falls only at $\sim 160^\circ$. The angular span of the pocket in θ can be more accurately

determined using a larger number of θ bins. The signal of anisotropy is strongest when the pocket is left empty and decreases when the pocket is filled with a homogeneous and isotropic Poisson distribution with a different density than the original one. We compare the degree of anisotropy when the pocket is filled with twice and half the density of the original distribution. It is interesting to note that the sig-

nals of anisotropy gets stronger with increasing density as it increases the disparity of the density inside the pocket from the original one. The anisotropy signals completely disappear when the pocket is filled with points having same density as the original one. In the left bottom panel we show the anisotropy as a function of azimuthal angle ϕ and similarly find $1 - \frac{H_\phi}{(H_\phi)_{max}} = 0$ for all ϕ values other than the range $90^\circ \leq \phi \leq 190^\circ$ where $1 - \frac{H_\phi}{(H_\phi)_{max}} > 0$ producing a bump in the azimuthal anisotropy in this ϕ range. This bump-like feature in the azimuthal anisotropy indicates violation of isotropy in the direction $90^\circ \leq \phi \leq 190^\circ$ in presence of the pocket. Interestingly the pocket introduced has the same angular span in ϕ . Clearly the bump does not appear in the absence of any such pocket. The bump height is maximum when the pocket is left empty. This can be explained from the fact that the empty pocket represents a situation where the region inside the pocket is most different from any other directions in the original distribution. The difference vanishes when the pocket has the same character and density as the original distribution. For any other density the bump would have an intermediate height between this two extreme situation. The presence of the pocket violates the isotropy of the distribution and is marked by the appearance of the bumps in the radial, polar and azimuthal anisotropies. Combining these information one can exactly infer the geometry of the pocket violating isotropy and also infer the degree of anisotropy due to it from the height of the bumps. Here we would like to mention that for an arbitrary shape of the pocket it is not trivial to figure out its exact geometry using the current method.

Next we consider the set of distributions where the pocket is filled with a homogeneous and isotropic Poisson distribution having density twice than that of the original one. We again separately measure anisotropies as a function of r , θ and ϕ from multiple points of observation inside the distribution. We shift the origin along x, y and z directions by $100h^{-1}$ Mpc without any rotation of the axes to have three different point of observations. We compare our findings in the top right, middle right and bottom right panels of Figure 2. In each of these cases we can probe only upto a radial distance of $r_{max} = 100h^{-1}$ Mpc as the original distribution extends upto a maximum distance of $200h^{-1}$ Mpc in the radial direction. In the top right panel of Figure 2 we show the anisotropy as a function of r for the cases where the centre is shifted along x, y or z directions or not shifted at all. We find that the variations in anisotropy are identical in all cases except when the origin is shifted along y direction. This is due to the fact that the geometry of the pocket ($80h^{-1}$ Mpc $\leq r \leq 180h^{-1}$ Mpc, $90^\circ \leq \theta \leq 140^\circ$, $90^\circ \leq \phi \leq 190^\circ$) does not affect the measurements in any of these cases other than when the shift is applied along y direction. This shows the existence of a preferred direction which clearly violates isotropy. This becomes even clearer in the right middle and right bottom panels of Figure 2. In the right middle panel we see that a bump appears between 90° to 160° when the centre is not shifted. In this case we considered the radius upto $r_{max} = 100h^{-1}$ Mpc even though we could extend it upto $200h^{-1}$ Mpc. This is due to the fact that we can only go upto this radius when the centre is shifted by $100h^{-1}$ Mpc. The pocket radially spans from $80 - 180h^{-1}$ Mpc and hence overlaps with the current measurement producing an anisotropy

signal in the appropriate range of θ . On the other hand the pocket is completely excluded from the measurements when the centre is shifted along x or z directions showing a near uniform very small signal of anisotropy for all θ values. This small signal of anisotropy arises due to the Poisson noise resulting simply from the reduction in the radial extensions of the volume elements used in the measurements. But when we shift the origin along y direction by $100h^{-1}$ Mpc the measurements include major part of the pocket showing anisotropy in the relevant range of θ . As there are no rotations of the axes, the bump appears exactly at $\theta = 90^\circ$ irrespective of whether the centre is shifted along y direction or not shifted at all. But the shifted position of the origin redefines the geometry of the pocket which changes the upper limit of θ for the pocket when the centre is shifted along y direction. We see very similar results in the right bottom panel of Figure 2 where anisotropies are shown as a function of ϕ . We again find presence of bumps over the appropriate range of ϕ values when the centre is shifted along y directions or not shifted at all whereas the distribution appears to be isotropic when the origin is shifted along x or z directions. These differences clearly indicate the presence of anisotropies in the distribution. The error-bars shown here in all the panels are the $1 - \sigma$ variations from the 10 Monte Carlo realizations used in each case.

For the inhomogeneous Poisson distributions the density only varies radially as $\frac{1}{r^2}$ from the centre. This preserves the isotropy of the distribution about the centre but isotropy is violated for all other points. We want to test if our method can capture the isotropy expected when viewed from the centre and quantify the anisotropies when the origin is shifted from the centre. The results are shown in different panels of Figure 3. In top left panel we show the anisotropy as a function of radial distance r when the origin is located at the centre of the spherical volume. When we compare the anisotropy in the homogeneous and radially inhomogeneous Poisson distributions we find that the former shows a higher degree of anisotropy than the later. The inhomogeneous Poisson distribution considered here has a radial variation in density as $\frac{1}{r^2}$ from the centre. As a result the number density of points are significantly higher at smaller radii in the inhomogeneous Poisson distribution as compared to the homogeneous one. This leads to significant reduction in the Poisson noise at smaller radii where it is considered to be more dominant. At larger radii the situation would be just opposite but as the number counts are cumulative in our method the distribution would remain isotropic as expected despite the radial decrease in density. In the middle left and bottom left panels of Figure 3 we show the anisotropies as function of θ and ϕ respectively. In both cases we have used $r_{max} = 200h^{-1}$ Mpc. We find that as expected the distributions are found to be highly isotropic from the centre.

In the top right panel we show the anisotropies as a function of r when we shift the origin from the centre by $100h^{-1}$ Mpc along x or y or z direction. For this we use $r_{max} = 100h^{-1}$ Mpc which is also used for the results shown in the middle right and bottom right panels of this figure. We see that the anisotropy increases drastically at smaller radii when the origin is shifted along x, y or z directions. The anisotropy decreases with increasing radii due to the relative increase in the number counts but soon increases afterwards due to large disparity in the density at the central and pe-

ripheral regions. Noticeably the variations in anisotropies are identical when the origin is shifted from the centre along x, y or z directions due to the identical variations in density along all radial directions but they are completely different from the results obtained without shifting the origin from the centre. This demonstrates the anisotropic nature of the distribution. The middle right panel show how the anisotropy varies as the polar angle θ when the origin is shifted in various directions. It is interesting to note that when we shift the origin along z direction the distribution appears to be isotropic in θ as it would appear without any shift at all. The relative Shannon entropy is measured across all the ϕ bins at each θ values. The polar angle θ is defined with respect to the z axis and all the ϕ bins at a specific θ value are located at the same distance from the centre. Since the density only changes in the radial directions the distribution would appear isotropic in all ϕ directions for each θ when the origin is shifted in the z direction. The situations are not analogous when the origin is shifted in the x or y direction. In both the cases different ϕ bins at any given θ value are located at different distances from the centre leading to variations in their densities. This is true for all θ values albeit with a different degree of variation. The degree of variation across all the ϕ bins is expected to peak at $\theta = 90^\circ$ as it would encompass largest variation in the radial distances among the ϕ bins. Interestingly our method capture these predictable behaviours of anisotropies as a function of polar angle θ quite well. Finally in the bottom right panel we show the anisotropies as a function of the azimuthal angle ϕ when the origin is shifted along the three different directions. Here we estimate the relative Shannon entropy utilizing the information across all the θ bins at each ϕ values. When the origin is shifted in z direction the azimuthal angle ϕ is redefined in the shifted x-y plane which lies at a fixed distance $100h^{-1}$ Mpc from the centre. Consequently different θ bins at any given ϕ value are at different distances from the centre leading to variations in their densities but the degree of variations across the different θ bins for each ϕ value would be exactly same as the θ bins cover same variations in their radial distances. In the bottom right panel we see a constant degree of anisotropy across all the ϕ values when the origin is shifted along z direction. On the other hand when the origin is shifted along x or y direction the available θ bins at each ϕ value are located at different distances from the centre. As a result the different θ bins at each ϕ values would exhibit different number density depending on their distances from the centre. But the degree of variations would not be same for all the ϕ bins as it depends both on the distance range covered by the corresponding θ bins and whether those θ bins lie towards or away from the centre. Clearly these variations are expected to peak at $\phi = 180^\circ$ and $\phi = 270^\circ$ for shift along x and y directions respectively. We exactly recover these predictable behaviours in the bottom right panel. Differences in the anisotropies with shifts and without shift clearly indicate that the distribution is anisotropic in nature. The results also point out that our method is not only able to sense the signals of anisotropy but also can capture the nature of anisotropies present in a distribution.

In [Figure 4](#) we investigate the anisotropies resulting from the redshift space distortions using a semi analytic galaxy catalogue from the Millennium Run simulation. In

the top left panel of this figure we compare the anisotropies as a function of radius r for the simulated galaxy distributions in real and redshift space. Both distributions show anisotropies on small scales which partly arise due to inevitable Poisson noise. The degree of anisotropy gradually decreases with increasing radii. Noticeably at smaller radii the degree of anisotropy in both the distributions are higher as compared to a homogeneous and isotropic Poisson distribution indicating the presence of additional sources of anisotropy other than the Poisson noise. We see that on smaller radii the redshift space distribution of the simulated galaxies are more anisotropic than its real space counterpart. This is most likely caused due to the elongation of virialized clusters, compression of large scale overdensities and elongation of large scale underdensities along the line of sight in redshift space. The results clearly indicate that distribution of galaxies inside the cosmic web is not isotropic even in real space and redshift space distortions only enhance these anisotropies further. The differences between the real space and redshift space anisotropies cease to exist beyond $40h^{-1}$ Mpc and both the anisotropies become almost indistinguishable from that observed in homogeneous and isotropic Poisson distributions at $\sim 140h^{-1}$ Mpc. It may be worth mentioning here that in an earlier work ([Pandey & Sarkar 2015](#)) we find that observed galaxy distribution in the SDSS DR12 appears to be homogeneous on scales above $140h^{-1}$ Mpc. In the middle left and bottom left panels of [Figure 4](#) we show the anisotropies as a function of θ and ϕ respectively. In both these panels we find that the real and redshift space distributions are equally isotropic in θ and ϕ . A small signal of anisotropy exist for both real and redshift space distributions of the simulated galaxies which separates them from identical homogeneous and isotropic Poisson distributions. The real and redshift space distributions demonstrate equal degree of isotropy both in θ and ϕ due to the fact that the compression and elongation of overdense and underdense regions are symmetric along the line of sight. We use $r_{max} = 200h^{-1}$ Mpc for all the results shown in all the panels on left of [Figure 4](#).

Now we shift the origin from the centre along the x or y or z axis by $100h^{-1}$ Mpc in the redshift space distribution of the simulated galaxies. The resulting anisotropies as a function of r , θ and ϕ are shown in the top right, middle right and bottom right panels of [Figure 4](#) respectively. We use $r_{max} = 100h^{-1}$ Mpc for these analyses. We see in the top right panel of [Figure 4](#) that the observed anisotropies change at smaller radii when the origin is shifted along x, y or z directions than when it is not shifted. This tells us that the distribution is anisotropic under such shifts. In the middle right and bottom right panels we show the anisotropies in analogous situations but as functions of θ and ϕ respectively. The results in these panels show that the resulting anisotropies under such shifts and without shift appears to be similar when measured as functions of θ and ϕ whereas the level of anisotropies are expected to be different in this case when the origin is shifted from the centre. The top right panel of [Figure 4](#) agrees quite well with this expected behaviour but the middle right and bottom right panels do not exhibit these differences. The redshift space distortions are caused by the radial component of peculiar velocities which distorts the structures along the line of sight. The method presented here may not be able to capture the anisotropies imprinted

in the details of distortions when looked in the polar and azimuthal directions as we are currently using only the number counts within the solid angle bins which radially extends upto r_{max} . Using the correlation functions instead of number counts may prove to be a better bet here.

We find that our method can identify various types of anisotropies and distinguish between them. But in general the distributions could be much more complex specially when the observed anisotropy is produced by different possible combinations of various types of anisotropies. Disentangling such anisotropies is no doubt would be quite challenging. However our method could serve the purpose of detecting anisotropies quite well. In future we plan to analyze data from the Two Micron All Sky Survey (2MASS) and the Sloan Digital Sky Survey (SDSS) to test the assumption of isotropy in the present Universe. The proposed method can be applied in many problems in Cosmology which requires testing of isotropy. For example it can be used to investigate the issues like the anisotropic distribution of galactic satellites (Zentner et al. 2005) and anisotropic distribution of subhalos inside dark matter halos and the cosmic web (Kang & Wang 2015). The method can be also used further to test for any hemispherical asymmetry in the angular distribution of galaxy clusters (Bengaly et al. 2015) and gamma-ray bursts (Briggs et al. 1996). One can also compute the luminosity functions and mass functions or determine various cosmological parameters in different directions and use them to test the presence of any hemispherical asymmetry using the method proposed in the present work. Finally we note that the method presented here has the desired ability to identify and characterize any signals of anisotropy present in a distribution and it can be also suitably adapted for different types of datasets from other cosmological observations to efficiently explore the issue of Cosmic isotropy.

5 ACKNOWLEDGEMENT

The author would like to acknowledge CTS, IIT Kharagpur for the use of its facilities for the present work. The author would also like to acknowledge IUCAA, Pune for providing support through the Associateship Programme.

The Millennium Simulation data bases (Lemson & Virgo Consortium 2006) used in this paper and the web application providing online access to them were constructed as part of the activities of the German Astrophysical Virtual Observatory.

REFERENCES

- Ahn, C. P., Alexandroff, R., Allende Prieto, C., et al. 2014, *ApJS*, 211, 17
- Alonso, D., Salvador, A. I., Sánchez, F. J., et al. 2015, *MNRAS*, 449, 670
- Appleby, S., & Shafieloo, A. 2014, *JCAP*, 10, 070
- Baugh, C.M., Cole, S., Frenk, C.S. & Lacey, C.G. 1998, *ApJ*, 498, 504
- Barrow, J. D., & Hervik, S. 2010, *Physical Review D*, 81, 023513
- Bengaly, C. A. P., Jr., Bernui, A., & Alcaniz, J. S. 2015, *ApJ*, 808, 39
- Bengaly, C. A. P., Jr., Bernui, A., Alcaniz, J. S., & Ferreira, I. S. 2015, arXiv:1511.09414
- Benson, A.J., Lacey, C.G., Baugh, C.M., Cole, S. & Frenk, C.S. 2002, *MNRAS*, 333, 156
- Bennett, C. L., Hill, R. S., Hinshaw, G., et al. 2011, *ApJS*, 192, 17
- Briggs, M. S., Paciasas, W. S., Pendleton, G. N., et al. 1996, *ApJ*, 459, 40
- Bruzual, G., & Charlot, S. 2003, *MNRAS*, 344, 1000
- Buchert, T., & Ehlers, J. 1997, *A&A*, 320, 1
- Buchert, T. 2001, *General Relativity and Gravitation*, 33, 1381
- Campanelli, L., Cea, P., Fogli, G. L., & Marrone, A. 2011, *Physical Review D*, 83, 103503
- Chan, R., da Silva, M. F. A., & Villas da Rocha, J. F. 2009, *Modern Physics Letters A*, 24, 1137
- Cole, S., Aragon-Salamanca, A., Frenk, C.S., Navarro, J.F., Zepf, S.E. 1994, *MNRAS*, 271, 781
- Cole, S., Lacey, C.G., Baugh, C.M. & Frenk, C.S. 2000, *MNRAS*, 319, 168
- Colin, J., Mohayaee, R., Sarkar, S., & Shafieloo, A. 2011, *MNRAS*, 414, 264
- Croton, D. J., Springel, V., White, S. D. M., et al. 2006, *MNRAS*, 365, 11
- Das, S., Mitra, S., Rotti, A., Pant, N., & Souradeep, T. 2014, arXiv:1401.7757
- Dai, L., Jeong, D., Kamionkowski, M., & Chluba, J. 2013, *Physical Review D*, 87, 123005
- De Lucia, G., & Blaizot, J. 2007, *MNRAS*, 375, 2
- Fang, K., & Linden, T. 2015, *Physical Review D*, 91, 083501
- Fixsen, D. J., Cheng, E. S., Gales, J. M., et al. 1996, *ApJ*, 473, 576
- Gruppuso, A., Natoli, P., Paci, F., et al. 2013, *JCAP*, 7, 047
- Gupta, S., & Saini, T. D. 2010, *MNRAS*, 407, 651
- Guo, Q., White, S., Boylan-Kolchin, M., et al. 2011, *MNRAS*, 413, 101
- Hajian, A., & Souradeep, T. 2003, *ApJ Letters*, 597, L5
- Hamilton, A.J.S. *ApJ*, 385, L5
- Hanson, D., & Lewis, A. 2009, *Physical Review D*, 80, 063004
- Huterer, D., Shafer, D. L., & Schmidt, F. 2015, arXiv:1509.04708
- Hazra, D. K., & Shafieloo, A. 2015, *JCAP*, 11, 012
- Jackson, J. C. 2012, *MNRAS*, 426, 779
- Javanmardi, B., Porciani, C., Kroupa, P., & Pflamm-Altenburg, J. 2015, *ApJ*, 810, 47
- Kaiser, N. 1987, *MNRAS*, 227, 1
- Kalus, B., Schwarz, D. J., Seikel, M., & Wiegand, A. 2013, *A&A*, 553, A56
- Kang, X., Wang, P. 2015, *ApJ*, 813, 6
- Kashlinsky, A., Atrio-Barandela, F., Kocevski, D., & Ebeling, H. 2008, *ApJ Letters*, 686, L49
- Kashlinsky, A., Atrio-Barandela, F., Ebeling, H., Edge, A., & Kocevski, D. 2010, *ApJ Letters*, 712, L81
- Kauffmann, G., White, S.D.M. & Guiderdoni, B. 1993, *MNRAS*, 264, 201
- Kauffmann, G. & White, S.D.M. 1993, *MNRAS*, 261, 921
- Kauffmann, G. 1996, *MNRAS*, 281, 487
- Kolb, E. W., Matarrese, S., & Riotto, A. 2006, *New Journal of Physics*, 8, 322
- Land, K., & Magueijo, J. 2005, *Physical Review Letters*, 95, 071301
- Lemson, G., & Virgo Consortium, t. 2006, arXiv:astro-ph/0608019
- Lin, H.-N., Wang, S., Chang, Z., & Li, X. 2015, Accepted in *MNRAS*, arXiv:1504.03428
- Marinoni, C., Bel, J., & Buzzi, A. 2012, *JCAP*, 10, 036
- Marozzi, G., & Uzan, J.-P. 2012, *Physical Review D*, 86, 063528
- Moss, A., Scott, D., Zibin, J. P., & Battye, R. 2011, *Physical Review D*, 84, 023014
- Mukherjee, S., Aluri, P. K., Das, S., Shaikh, S., & Souradeep, T. 2015, arXiv:1510.00154
- Pandey, B. 2013, *MNRAS*, 430, 3376

- Pandey, B., & Sarkar, S. 2015, MNRAS, 454, 2647
- Penzias, A. A., & Wilson, R. W. 1965, ApJ, 142, 419
- Pitrou, C., Pereira, T. S., & Uzan, J.-P. 2008, JCAP, 4, 004
- Planck Collaboration, Ade, P. A. R., Aghanim, N., et al. 2014, A&A, 571, A23
- Planck Collaboration, Ade, P. A. R., Aghanim, N., et al. 2015, arXiv:1506.07135
- Schwarz, D. J., Starkman, G. D., Huterer, D., & Copi, C. J. 2004, Physical Review Letters, 93, 221301
- Schwarz, D. J., & Weinhorst, B. 2007, A&A, 474, 717
- Shannon, C. E. 1948, Bell System Technical Journal, 27, 379-423, 623-656
- Shtanov, Y. 2010, Annalen der Physik, 522, 332
- Smoot, G. F., Bennett, C. L., Kogut, A., et al. 1992, ApJ Letters, 396, L1
- Soda, J. 2012, Classical and Quantum Gravity, 29, 083001
- Somerville, R.S. & Primack, J.R. 1999, MNRAS, 310, 1087
- Springel, V., White, S. D. M., Jenkins, A., et al. 2005, Nature, 435, 629
- Taylor, S. R., & Gair, J. R. 2013, Physical Review D, 88, 084001
- Watkins, R., Feldman, H. A., & Hudson, M. J. 2009, MNRAS, 392, 743
- White, S. D. M. & Frenk, C. S. 1991, ApJ, 379, 52
- Wilson, R. W., & Penzias, A. A. 1967, Science, 156, 1100
- Zentner, A. R., Kravtsov, A. V., Gnedin, O. Y., & Klypin, A. A. 2005, ApJ, 629, 219
- Zunckel, C., Huterer, D., & Starkman, G. D. 2011, Physical Review D, 84, 043005

This paper has been typeset from a $\text{\TeX}/\text{\LaTeX}$ file prepared by the author.